Many-body effects in doped graphene on a piezoelectric substrate

David G. González,[1,2,*] Ivar Zapata,[1] Jürgen Schiefele,[1,3] Fernando Sols,[1,2] and Francisco Guinea[4,5]
[1]*Departamento de Física de Materiales, Universidad Complutense de Madrid, E-28040 Madrid, Spain*
[2]*Campus de Excelencia Internacional, Campus Moncloa UCM-UPM, E-28040 Madrid, Spain*
[3]*Instituto de Ciencia de Materiales de Madrid, CSIC, E-28 049 Madrid, Spain*
[4]*IMDEA Nanociencia, Calle de Faraday 9, E-28 049 Madrid, Spain*
[5]*Department of Physics and Astronomy, University of Manchester, Oxford Road, Manchester M13 9PL, United Kingdom*
(Received 27 March 2017; revised manuscript received 16 August 2017; published 12 September 2017)

We investigate the many-body properties of graphene on top of a piezoelectric substrate, focusing on the interaction between graphene electrons and piezoelectric acoustic phonons. We calculate the electron and phonon self-energies as well as the electron mobility limited by the substrate phonons. We emphasize the importance of proper screening of the electron-phonon vertex, and we discuss the various limiting behaviors as a function of electron energy, temperature, and doping level. The effect of piezoelectric acoustic phonons on graphene electrons is compared with that of intrinsic deformation acoustic phonons. Substrate phonons tend to dominate over intrinsic ones for low doping levels at high and low temperatures.

DOI: 10.1103/PhysRevB.96.125119

I. INTRODUCTION

Elastic waves supported by the boundaries of solids and, in particular, surface acoustic waves (SAWs) underlie numerous applications of microwave devices for signal processing [1]. SAWs with amplitudes of a few nanometers can be electrically excited on the surface of piezoelectric materials, and the resulting periodic deformation in adjacent thin film materials or quantum-well structures can be employed to modulate optical resonances in polaritonic or plasmonic devices [2–4]. Apart from the mechanical deformation, the vibration of the ionic lattice in a piezoelectric material produces an electric field traveling along with the SAW, which can transport charge carriers in monolayer graphene deposited on top of the piezomaterial [5–7] and, for instance, probe graphene's Landau level structure when an external magnetic field is applied [8].

Because the carbon allotrope graphene is an atomically thin all-surface material [9], its charge-carrier dynamics is very sensitive to the surrounding electromagnetic fields, and the possibility of changing graphene's carrier concentration *in situ* by applying an external gate voltage is a key feature in many graphene-based devices [10]. Ballistic charge transport in suspended graphene over micrometer distances and unprecedented carrier mobilities [11] are enabled by the high frequencies of the optical phonons in the stiff honeycomb lattice. Thus, the effects of electron-phonon scattering on transport are small in comparison with conventional metals [9]. However, in most device architectures, graphene is deposited on a substrate, and all lattice modes of the substrate material that induce an electric field will influence the carriers in the graphene sheet, making the choice of substrate material crucial for the resulting transport characteristics of the device [12]. This mechanism of remote phonon scattering in graphene has been mainly studied for substrates supporting optical phonon modes [13–21].

In the present work, we aim to clarify the role of acoustic piezoelectric surface phonons, which form the microscopic quanta of SAWs [22], in graphene-on-piezomaterial structures. After analyzing within a diagrammatic framework the effective carrier interaction due to an exchange of surface phonons in Sec. II, we study the self-energies acquired by both phonons and charge carriers in Secs. III and IV. While the renormalization of the Fermi velocity due to piezoelectric substrate phonons turns out to be small, we show that there are regimes where the substrate effects dominate the momentum relaxation mechanism in graphene. We compare both lifetimes and mobilities with the results obtained when only intrinsic acoustic deformation phonons are considered. The numerical results for mean free paths and electron mobilities shown in Sec. V are applicable to a variety of piezoelectric materials with different lattice structures and piezoelectric strengths.

Our study can be relevant for graphene devices operating in the ballistic transport regime, such as hot electron transistor devices [23] or field-effect transistors based on graphene on different piezoelectrics [24,25], and for scenarios in which quantum interference induces localization phenomena [26].

II. EFFECTIVE ELECTRON-ELECTRON INTERACTION

A. Piezoelectric substrate

The sound velocities $v_s(\theta)$ of piezoelectric acoustic phonons are anisotropic (depending on the direction angle θ) and typically two or three orders of magnitude smaller than the Fermi velocity v_F in graphene, which yields a relatively low value of the maximum acoustic frequency. Thus the dielectric screening effects due to the substrate can be described by its static (also anisotropic) dielectric constant $\varepsilon_0(\theta)$. This constant combines both core excitons and optical phonons as well as any high-frequency (instantaneous) polarization forces that screen the fields created by the piezoelectric acoustic phonons [27]. The Fourier transform of the repulsive Coulomb interaction thus reads

$$v_{\mathbf{q}}^{(0)} = \frac{2\pi e^2}{\bar{\varepsilon}_0(\theta) q}, \tag{1}$$

*d.gonzalez@mat.ucm.es

where $\bar{\varepsilon}_0(\theta) = \frac{\varepsilon_0(\theta)+1}{2}$ is the effective dielectric constant at the substrate-air interface [28], and $q = |\mathbf{q}|$ with $\mathbf{q} = (q_x, q_y)$ and $\theta \equiv \arg(q_x + iq_y)$.

The interaction between the graphene electrons and the piezoelectric acoustic (PA) phonons is given by

$$H_{e\text{-ph}}^{\text{PA}} = \frac{1}{\sqrt{A}} \sum_{\mathbf{k},\mathbf{q},\sigma} \gamma_{\mathbf{q}}^{\text{PA}}\, a_{\mathbf{k}+\mathbf{q},\sigma}^{\dagger} a_{\mathbf{k},\sigma} b_{\mathbf{q}} + \text{H.c.} \tag{2}$$

Here, A is the sample area, and $a_{\mathbf{k},\sigma}$ is the Fermi operator for an electron of wave vector $\hbar\mathbf{k}$, spin-valley-cone index σ, and energy

$$E_{k\sigma} = \hbar s v_F k, \tag{3}$$

where $s = \pm 1$ is the cone index; $b_{\mathbf{q}}$ is the Bose operator for a substrate PA phonon of wave vector $\mathbf{q}$ and (direction-dependent) frequency

$$\omega_{\mathbf{q}} = v_s(\theta) q. \tag{4}$$

As in Ref. [29], where a general form of the piezoelectric acoustic-phonon–electron interaction was derived (and compared to the general Fröhlich interaction with optical phonons), we assume that we only have to deal with phonons of momentum much smaller than the piezoelectric inverse lattice spacing (elastic limit). The electron-phonon coupling is then characterized by the q-independent vertex

$$\gamma_{\mathbf{q}}^{\text{PA}} = K_R(\theta) \left[\frac{\pi \alpha_{\text{fs}} \hbar^2 v_F v_s(\theta)}{\bar{\varepsilon}_0(\theta)} \right]^{\frac{1}{2}}, \tag{5}$$

where $\alpha_{\text{fs}} = e^2/(\hbar v_F) \simeq 2.2$. It should be understood that, in the absence of the substrate, we are in the usual Fermi liquid regime of (doped) graphene. Quite generally, the electromechanical coupling coefficient satisfies $K_R(\theta) < 1$. The general derivation of Eq. (5) is discussed in Ref. [29].

The coupling Eq. (5) enables a phonon-mediated electron-electron interaction

$$V_{\text{ph}}^{\text{PA}}(\mathbf{q},\omega) = \left|\gamma_{\mathbf{q}}^{\text{PA}}\right|^2 G_0^{\text{PA}}(\mathbf{q},\omega), \tag{6}$$

where

$$G_0^{\text{PA}}(\mathbf{q},\omega) = \frac{2\omega_{\mathbf{q}}/\hbar}{\omega^2 - \omega_{\mathbf{q}}^2 + i0^+} \tag{7}$$

denotes the bare propagator of the surface acoustic phonons. By including screening effects due to the charge carriers in graphene, as described by the polarization $\Pi_0(q,\omega)$ (see Refs. [30,31]), we can define the total effective electron-electron interaction in terms of an anisotropic dielectric function $\varepsilon(\mathbf{q},\omega)$:

$$\begin{aligned} V_{\text{eff}}(\mathbf{q},\omega) &= \frac{2\pi e^2}{\varepsilon(\mathbf{q},\omega) q} \\ &= \frac{v_{\mathbf{q}}^{(0)} + V_{\text{ph}}^{\text{PA}}(\mathbf{q},\omega)}{1 - \left[v_{\mathbf{q}}^{(0)} + V_{\text{ph}}^{\text{PA}}(\mathbf{q},\omega)\right] \Pi_0(q,\omega)}. \end{aligned} \tag{8}$$

Here and in the following, we adopt the convention of referring to q as a subindex or argument when the dependence on $\mathbf{q}$ has circular symmetry. For low enough frequencies, typically $\hbar\omega \ll k_B T_{\text{BG}}$, where T_{BG} is the Bloch-Grüneisen temperature [defined in Eq. (40)], the phonon-induced electron-electron interaction adopts a q dependence similar to that of the Coulomb interaction:

$$V_{\text{ph}}^{\text{PA}}(\mathbf{q},\omega) \simeq -\frac{2\left|\gamma_{\mathbf{q}}^{\text{PA}}\right|^2}{\hbar v_s q}. \tag{9}$$

By defining

$$\varepsilon_{\text{RPA}}(\mathbf{q},\omega) = 1 - v_{\mathbf{q}}^{(0)} \Pi_0(q,\omega), \tag{10}$$

we obtain for $\omega \to 0$

$$\varepsilon_{\text{RPA}}(\mathbf{q},\omega) \simeq \varepsilon_{\text{RPA}}(\mathbf{q},0), \tag{11}$$

where the static dielectric function satisfies

$$\varepsilon_{\text{RPA}}(\mathbf{q},0) = 1 + \frac{k_{\text{TF}}(\theta)}{q} \tag{12}$$

for $q < 2k_F$, where

$$k_{\text{TF}} = \frac{4\alpha_{\text{fs}} k_F}{\bar{\varepsilon}_0(\theta)} \tag{13}$$

is the (anisotropic) Thomas-Fermi wave vector and k_F is the Fermi wave vector, the factor of 4 accounting for spin-valley degeneracy.

We may also define the renormalized phonon propagator

$$\tilde{G}^{\text{PA}}(\mathbf{q},\omega) = \frac{G_0^{\text{PA}}(\mathbf{q},\omega)}{1 - \frac{V_{\text{ph}}^{\text{PA}}(\mathbf{q},\omega)\Pi_0(q,\omega)}{\varepsilon_{\text{RPA}}(\mathbf{q},\omega)}}. \tag{14}$$

Then, Eq. (8) can be decomposed into an electron-electron and an electron-phonon part [27,32]. We obtain [29]

$$V_{\text{eff}}(\mathbf{q},\omega) = \frac{v_{\mathbf{q}}^{(0)}}{\varepsilon_{\text{RPA}}(\mathbf{q},\omega)} + \left|\frac{\gamma_{\mathbf{q}}^{\text{PA}}}{\varepsilon_{\text{RPA}}(\mathbf{q},\omega)}\right|^2 \tilde{G}^{\text{PA}}(\mathbf{q},\omega), \tag{15}$$

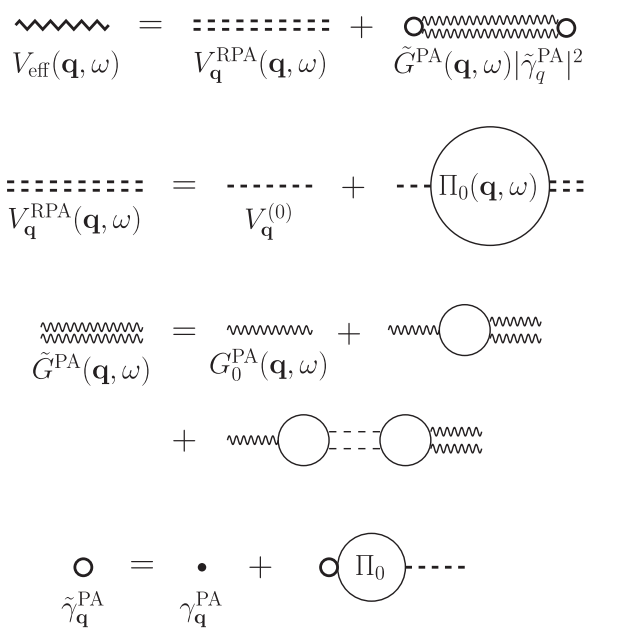

FIG. 1. Equivalent RPA scheme for the effective electron-electron interaction separated into an electron-electron Coulombic part and an electron-phonon part with a screened vertex and renormalized phonon propagator. In the second line, $V^{\text{RPA}}(\mathbf{q},\omega)$ is the first term of Eq. (15)

TABLE I. Angle-averaged values of the electromechanical coupling coefficient K_R^2 appearing in Eq. (5), the effective dielectric constant $\bar{\varepsilon}_0$, the sound velocity v_s, the vertex strength $\gamma_{\mathbf{q}}^{\mathrm{PA}}$ [see Eq. (5)], the dimensionless coupling strength $\lambda_{e\text{-ph}}$ defined in Eq. (17), and the ratio k_{TF}/k_F for several materials. Numerical values of the elastic, piezoelectric, and dielectric tensors have been taken from Refs. [33–35] and references therein.

Material	Cut	K_R^2	$\bar{\varepsilon}_0$	$v_s\left(\frac{\mathrm{cm}}{\mathrm{s}}\right)$	$\lvert\gamma_{\mathbf{q}}^{\mathrm{PA}}\rvert^2$ (eV cm)^2	$\lambda_{e\text{-ph}}$	$4r_s$
GaAs (cubic)	X-Y-Z	0.0015	6.9	2.70×10^5	1.71×10^{-20}	0.0019	1.3
ZnO (6 mm)	Z cut	0.016	4.8	2.71×10^5	2.70×10^{-19}	0.029	1.8
ZnO (6 mm)	X cut	0.0064	4.8	2.63×10^5	6.60×10^{-20}	0.0074	1.8
AlN (6 mm)	Z cut	0.0026	5.0	5.85×10^5	9.18×10^{-20}	0.0046	1.8
AlN (6 mm)	X cut	0.0048	5.0	5.81×10^5	1.66×10^{-19}	0.0084	1.8
$LiNbO_3$ (3 m)	Z cut	0.0068	19	3.85×10^5	4.25×10^{-20}	0.0032	0.46
$LiNbO_3$ (3 m)	Y cut	0.017	20	3.59×10^5	9.35×10^{-20}	0.0077	0.44
$LiNbO_3$ (3 m)	X cut	0.019	20	3.60×10^5	9.80×10^{-20}	0.0080	0.44
PZT-4 (6 mm)	Z cut	0.027	350	2.26×10^5	5.37×10^{-21}	7.0×10^{-4}	0.025
PZT-4 (6 mm)	X cut	0.0021	350	1.80×10^5	3.17×10^{-22}	5.2×10^{-5}	0.025

as shown diagrammatically in Fig. 1. We wish to emphasize the importance of electronic screening of the electron-phonon vertex shown in Eq. (15). This will strongly influence the role of scattering processes involving low values of q.

B. Input parameters and main approximations

The input parameters of our study are those that characterize the piezoelectric substrate, namely $K_R(\theta)$, $v_s(\theta)$, and $\bar{\varepsilon}_0(\theta)$, from which the electron-phonon interaction $\gamma_{\mathbf{q}}^{\mathrm{PA}}(\theta)$ is computed [see Eq. (5)]. On the other hand, the graphene electron system is characterized by its doping level as given by k_F. A dimensionless parameter $\lambda_{e\text{-ph}}(\theta)$ characterizing the strength of the coupling of Eqs. (5) and (9) can be obtained from multiplying the resulting effective interaction (6) at $q = k_F$ by the density of states at the Fermi energy,

$$D(E_F) = -\Pi_0(k_F,0) = \frac{2k_F}{\pi\hbar v_F}, \tag{16}$$

which leads to

$$\lambda_{e\text{-ph}}(\theta) \equiv V_{\mathrm{ph}}^{\mathrm{PA}}(k_F\hat{\mathbf{q}},0)\Pi_0(k_F,0) = \frac{4}{\pi\hbar^2 v_s v_F}\left|\gamma_{\mathbf{q}}^{\mathrm{PA}}\right|^2 = 4K_R^2(\theta)r_s(\theta), \tag{17}$$

where $\hat{\mathbf{q}} = \mathbf{q}/q$ and the parameter

$$r_s(\theta) \equiv \frac{\alpha_{\mathrm{fs}}}{\bar{\varepsilon}_0(\theta)} \tag{18}$$

characterizes the ratio between the interaction and kinetic energies. This yields for the ratio between the piezoelectric interaction and the residual static Coulomb repulsion [29]

$$\frac{\lambda_{e\text{-ph}}}{\lambda_{e\text{-}e}} = K_R^2, \tag{19}$$

where

$$\lambda_{e\text{-}e}(\theta) = v_{k_F\hat{\mathbf{q}}}^{(0)}\Pi(k_F,0) = \frac{4\alpha_{\mathrm{fs}}}{\bar{\varepsilon}_0(\theta)} = 4r_s(\theta) \tag{20}$$

is the dimensionless electron-electron coupling strength in substrate-screened graphene.

The electromechanical coupling coefficient $K_R(\theta)$, characteristic of each piezoelectric material, can be measured in SAW experiments. It depends on the material's piezoelectric, elastic, and dielectric tensors, as well as on its mass density. In Table I we summarize angle-averaged values for selected representative materials as computed from the data given in Refs. [33–35].

For example, the materials considered in Ref. [4], namely ZnO and AlN, have associated piezoelectric tensors that are much larger than those of GaAs [36], which increases the electron-phonon coupling by more than one order of magnitude. But there exist piezoelectric materials whose coefficients are even larger, such as, e.g., $LiNbO_3$, $BaTiO_3$, or the PZT (lead zirconate titanate) $PbTi_xZr_{1-x}O_3$, among many oxides with the perovskite structure and formula ABO_3, which tend to show ferroelectric properties, and they are sometimes reminiscent of the layers between CuO_2 planes in cuprate high-temperature superconductors. Despite being more piezoelectric, the dielectric tensors in these ferroelectrics are so high that the interaction decreases [but not the ratio to the also highly screened Coulomb repulsion; see Eq. (19)]. We recall in this regard that, roughly, $K_R^2 \sim \hat{e}^2/(\hat{c}\bar{\varepsilon}_0)$, where $\hat{e}$ is a value for the piezoelectric tensor and $\hat{c}$ for the elastic tensor [37].

The point group of ZnO and AlN gives isotropic couplings with the Z cut and therefore isotropic sound velocities. On the other hand, their X and Y cuts are equivalent. This does not happen, for example, in $LiNbO_3$, whose $K_R^2(\theta)$ and vertex values in the X, Y, and Z cuts are shown in Fig. 2 as an example. For some graphs of the velocities in different cuts, see, for example, Ref. [38]. Here the cut refers to the lattice axis perpendicular to the surface; for a detailed description of the cut terminology, see, e.g., Refs. [39,40].

In the previous subsection, we have introduced the approximation of assuming a flat interface and taking the elastic (long phonon wavelength) limit for the piezoelectric, as expressed in Eq. (5) and used in Ref. [29]. We will also make the common assumption that the interface is large enough to permit the neglect of geometrical effects due to finite-size boundaries. This is expected to be a good approximation for system sizes much larger than the length scales of the problem, namely k_F^{-1} and k_{TF}^{-1}. In the discussion of analytical limits, as well as in the tractable computation of scattering rates, we will often take angle-averaged substrate parameters.

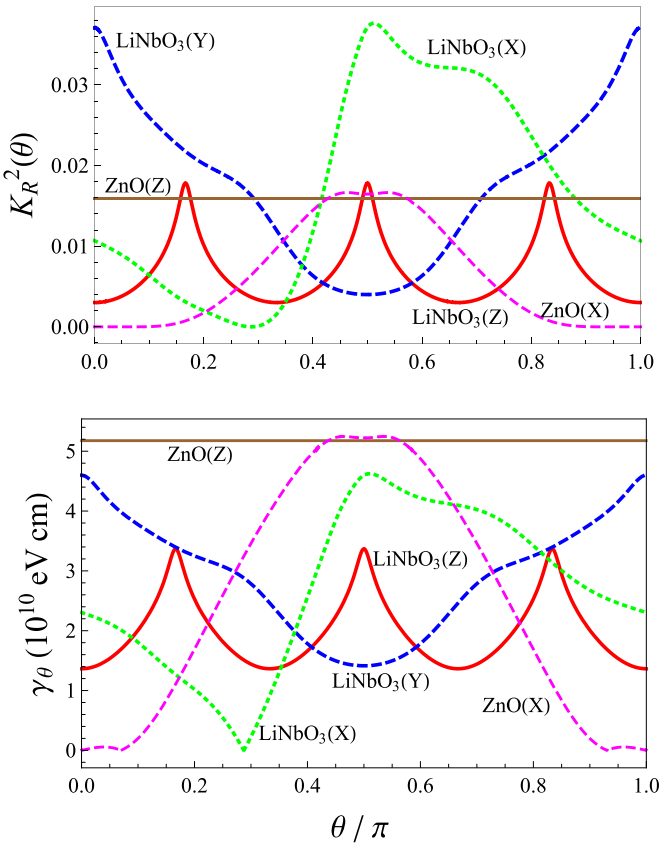

FIG. 2. Some representative magnitudes for SAW phonons and for two different materials with different symmetries ($LiNbO_3$ and ZnO), as a function of the angle within the crystal plane parallel to the cut plane, in the X-Y-Z cuts (denoted between parentheses). For the Z cut (X cut/Y cut), the zero angle corresponds to the x axis (y axis/z axis) with the angle growing toward the y axis (z axis/x axis). See Refs. [39,40] for a further account of the cut language convention. Upper: electromechanical coupling coefficient. Lower: electron-phonon vertex. The plots are obtained by processing data for the elastic, piezoelectric, and dielectric tensors taken from Refs. [33–35] and references therein.

III. PHONON SELF-ENERGY

As the piezoelectric coupling Eq. (2) enables the transfer of energy between carriers in graphene and the phonon modes of the substrate material, the latter acquire an extra decay rate due to Landau damping. To assess the magnitude of this effect, we proceed to estimate the self-energy of the substrate phonons due to their interactions with graphene carriers. Substituting the bare propagator (7) into (14), we obtain

$$\tilde{G}^{\rm PA}(\mathbf{q},\omega) = \frac{2\omega_{\mathbf{q}}/\hbar}{\omega^2 - \omega_{\mathbf{q}}^2 - 2\hbar^{-1}\omega_{\mathbf{q}}\left|\gamma_{\mathbf{q}}^{\rm PA}\right|^2 \frac{\Pi_0(q,\omega)}{\varepsilon_{\rm RPA}(\mathbf{q},\omega)}}. \tag{21}$$

In the phonon frequency range $\omega \sim v_s q \ll v_F q$ in which we will be mostly interested, we can approximate (see, e.g., Ref. [26])

$$\Pi_0(q,\omega) \simeq -D(E_F)\left(1 + i\frac{\omega}{v_F q}\right) \tag{22}$$

in the RPA electron-electron dielectric function Eq. (10), so that, in terms of the parameter $\lambda_{e\text{-ph}}(\theta)$, the poles of $\tilde{G}^{\rm PA}$ are shifted to

$$\tilde{\omega}_{\mathbf{q}} = \pm v_s q\left(1 - \lambda_{e\text{-ph}}\frac{k_F}{q + k_{\rm TF}}\right)^{\frac{1}{2}} \mp i\lambda_{e\text{-ph}}\frac{v_s}{v_F}\frac{v_s k_F}{2}\left(\frac{q}{q + k_{\rm TF}}\right)^2. \tag{23}$$

In the long-wavelength limit ($q \ll k_F$), the leading order of the ratio of the imaginary and real parts of the dressed phononic energy goes like

$$\left|\frac{{\rm Im}(\tilde{\omega}_{\mathbf{q}})}{{\rm Re}(\tilde{\omega}_{\mathbf{q}})}\right| \simeq \frac{1}{2}K_R^2\frac{v_s}{v_F}\left(\frac{q}{k_{\rm TF}}\right)^{\pm 1}, \tag{24}$$

where $(q/k_{\rm TF})^{\pm 1} \ll 1$, the case $k_{\rm TF} \ll q \ll k_F$ being meaningful only in those materials where $k_{\rm TF}$ is substantially smaller than k_F. Due to the fact that $v_F/v_s \sim 300$ and to the $K_R^2(\theta)$ values shown in Table I for typical materials, the lifetime of the phonons can be neglected in all analyzed regimes. It can also be shown that, near the quasiparticle poles, the residue $Z_{\mathbf{q}}$ is close to unity (i.e., the wave-function renormalization is weak):

$$\tilde{G}^{\rm PA}(\mathbf{q},\omega) \simeq Z_{\mathbf{q}}\frac{2\tilde{\omega}_{\mathbf{q}}/\hbar}{\omega^2 - \tilde{\omega}_{\mathbf{q}}^2}, \tag{25}$$

$$Z_{\mathbf{q}} \simeq 1 + \lambda_{\rm e\text{-}ph}\frac{k_F}{q + k_{\rm TF}}. \tag{26}$$

Thus in the following we can assume the substrate phonons to be well-defined, stable quasiparticles, and we will approximate the renormalized phonon propagator (25) by the bare one, Eq. (7).

IV. ELECTRON SELF-ENERGY

A. General expressions

We focus on the case of n-doped graphene ($E_F > 0$) so that we will be interested in the electron self-energies at energies $\hbar\omega$ in the upper Dirac cone. With an effective electron-electron interaction $V_{\rm eff}$ given in (15), the self-energy acquired by the charge carriers in graphene (within the G_0W approximation, as indicated in Fig. 3) has the general form

$$\Sigma_+(\mathbf{k},i\omega_n) = -k_B T\sum_{s=\pm}\sum_{\mathbf{q}}\sum_{i\nu_n} F_{+s}(\mathbf{k},\mathbf{k}+\mathbf{q}) \times G_{0,s}^{\rm el}(\mathbf{k}+\mathbf{q},i\omega_n + i\nu_n)V_{\rm eff}(\mathbf{q},i\nu_n), \tag{27}$$

where the subscript $+$ refers to the conduction band (the calculation for Σ_- being analogous), the index $s = \pm$ is summed over both bands,

$$G_{0,s}^{\rm el}(\mathbf{k},\omega) = (\omega - E_{\mathbf{k}s} - \mu)^{-1} \tag{28}$$

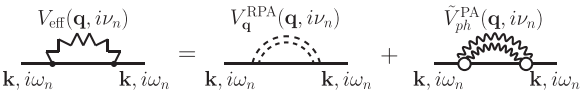

FIG. 3. Electron self-energy in the G_0W approximation; see Eq. (27).

denotes the (bare) electron propagator, $i\nu_n$ and $i\omega_n$ are, respectively, the bosonic and fermionic Matsubara frequencies, and the spinor overlap factor

$$F_{+s}(\mathbf{k},\mathbf{k}+\mathbf{q}) = \tfrac{1}{2}(1+s\cos\alpha) \tag{29}$$

arises due to the sublattice structure of graphene [9], α being the angle formed by $\mathbf{k}$ and $\mathbf{k}+\mathbf{q}$.

Expression (15) for $V_{\rm eff}$ allows us to separate the self-energy Σ_+ into contributions due to electron-electron and electron-phonon interactions. While the former has been considered in Refs. [26,41], the contributions of graphene-intrinsic optical or acoustic phonons, as well as optical substrate phonons, to the electron self-energy have been studied in Refs. [21,26]. Thus in the present work we focus entirely on the effect of piezoelectric acoustic substrate phonons, as expressed in the self-energy

$$\Sigma_+^{\rm PA}(\mathbf{k},i\omega_n) = -k_BT\sum_{s=\pm}\sum_{\mathbf{q}}\sum_{i\nu_n} F_{+s}(\mathbf{k},\mathbf{k}+\mathbf{q}) \times G^{\rm el}_{0,+}(\mathbf{k}+\mathbf{q},i\omega_n+i\nu_n)\tilde{V}^{\rm PA}_{\rm ph}(\mathbf{q},i\nu_n), \tag{30}$$

where

$$\tilde{V}^{\rm PA}_{\rm ph}(\mathbf{q},\omega) \equiv \left|\frac{\gamma^{\rm PA}_{\mathbf{q}}}{\varepsilon_{\rm RPA}(\mathbf{q},\omega)}\right|^2 \tilde{G}^{\rm PA}(\mathbf{q},\omega). \tag{31}$$

To sum over over Matsubara frequencies, we follow Ref. [27] and approximate the vertex renormalization by its static limit [see Eq. (12)] while neglecting the phonon self-energy, i.e., in Eq. (30) we replace $\tilde{V}^{\rm PA}_{\rm ph}(\mathbf{q},\omega)$ by

$$\bar{V}^{\rm PA}_{\rm ph}(\mathbf{q},\omega) \equiv \left|\frac{\gamma^{\rm PA}_{\mathbf{q}}}{\varepsilon_{\rm RPA}(\mathbf{q},0)}\right|^2 G^{\rm PA}_0(\mathbf{q},\omega). \tag{32}$$

We arrive at the following retarded self-energy:

$$\Sigma_+^{\rm PA}(\mathbf{k},\omega) = \sum_{s=\pm}\int\frac{d\mathbf{q}}{(2\pi)^2}\left|\frac{\gamma^{\rm PA}_{\mathbf{q}}}{\varepsilon_{\rm RPA}(\mathbf{q},0)}\right|^2 F_{+s}(\mathbf{k},\mathbf{k}') \times\left[\frac{n_B(\hbar\omega_{\mathbf{q}})+n_F(\epsilon_{k's})}{\hbar\omega+\hbar\omega_{\mathbf{q}}-\epsilon_{k's}+i0^+} + \frac{n_B(\hbar\omega_{\mathbf{q}})+1-n_F(\epsilon_{k's})}{\hbar\omega-\hbar\omega_{\mathbf{q}}-\epsilon_{k's}+i0^+}\right], \tag{33}$$

where $\mathbf{k}'$ stands for $\mathbf{k}'\equiv\mathbf{k}+\mathbf{q}$,

$$n_B(\hbar\omega_{\mathbf{q}}) = \left[\exp\left(\frac{\hbar\omega_{\mathbf{q}}}{k_BT}\right)-1\right]^{-1}, \tag{34}$$

$$n_F(\epsilon_{k's}) = \left[\exp\left(\frac{\epsilon_{k's}}{k_BT}\right)+1\right]^{-1} \tag{35}$$

denote the Bose and Fermi distributions, respectively, and the energies $\epsilon_{ks}=E_{ks}-\mu$ are taken relative to the chemical potential. We proceed by evaluating the real and imaginary parts of Eq. (33) separately. Hereafter, we assume $T\ll T_F$ so that the zero-temperature RPA dielectric function can be used [30]. Since $\mu\simeq E_F$, we can write

$$\epsilon_{ks} = \hbar v_F(ks-k_F). \tag{36}$$

B. Imaginary part

The imaginary part of Eq. (33) acquires the form

$$\mathrm{Im}\,\Sigma_+^{\rm PA}(\mathbf{k},\omega) = -\pi\sum_{s=\pm}\sum_{t=\pm}\int\frac{d\mathbf{q}}{(2\pi)^2}\left|\frac{\gamma^{\rm PA}_{\mathbf{q}}}{\varepsilon_{\rm RPA}(\mathbf{q},0)}\right|^2\frac{1+s\cos\alpha}{2} \times[n_F(\hbar\omega_{\mathbf{q}}+t\hbar\omega)+n_B(\hbar\omega_{\mathbf{q}})] \times\delta(\hbar\omega+t\hbar\omega_{\mathbf{q}}-\epsilon_{k's}), \tag{37}$$

where $t=\pm1$ corresponds to the absorption or emission of a phonon, respectively.

Setting $\omega=\epsilon_{k+}$ in Eq. (37), that is, considering the on-shell self-energy, yields the value $\hbar/(2\tau)$ for the decay width of charge carriers with wave vector $\mathbf{k}$. Here we are assuming that the renormalization of the Fermi energy $\Delta E_F = \mathrm{Re}\,\Sigma^{\rm PA}(k_F,0)$, as given by the pole of the dressed electron propagator, is tiny, as can be checked in the next section [see Eq. (58) and related ones]. To obtain analytical expressions for the asymptotic behaviors of the on-shell self-energy, we introduce the quasielastic approximation

$$\delta(\epsilon_{k+}+t\hbar\omega_{\mathbf{q}}-\epsilon_{k's}) \simeq \delta(\epsilon_{k+}-\epsilon_{k's}) \tag{38}$$

in Eq. (37), which is well justified since $v_F/v_s\sim300$. As we are working with $k_F>0$, the $s=-$ term is null. Hereafter, ϵ_k will be equivalent to ϵ_{k+}, so that

$$\epsilon_k = \hbar v_F(k-k_F). \tag{39}$$

For magnitude estimates, we will assume $\epsilon_k>0$.

The relevant scale for finite-temperature effects in graphene, where carrier densities are much smaller than in conventional metals, is the Bloch-Grüneisen temperature $T_{\rm BG}$, defined as the scale of the acoustic phonons in the Fermi sea,

$$k_BT_{\rm BG} \equiv 2\hbar v_sk_F. \tag{40}$$

1. Zero temperature, small k

Then at zero temperature (by which we mean $T\ll\epsilon_k/k_B,T_{\rm BG}$), n_F in (37) becomes a step function that cuts off the momentum integration, while n_B vanishes. Then, in the limit $\epsilon_k\ll\hbar v_sk_{\rm TF}$ [for which the largest contributing q in (37) is $q\sim\epsilon_k/\hbar v_s$ so that we can assert $q\ll k_{\rm TF}$] the quasiparticle lifetime decays as ϵ_k^3 near the Fermi surface while depending on the direction of the $\mathbf{k}$ vector:

$$-\mathrm{Im}\,\Sigma_+^{\rm PA}(\mathbf{k},\epsilon_k) \simeq \frac{1}{6\pi}\frac{|\gamma^{\rm PA}_\perp|^2}{\hbar v_Fk^2_{\rm TF\perp}}\frac{\epsilon_k^3}{(\hbar v_{s\perp})^3} = \frac{\lambda_\perp}{24}\left(\frac{k_F}{k_{\rm TF\perp}}\right)^2\left(\frac{v_F}{v_{s\perp}}\right)^2\left(\frac{\epsilon_k}{E_F}\right)^3\hbar v_Fk_F, \tag{41}$$

where all the substrate-related constants, like $\lambda_\perp\equiv\lambda_{\text{e-ph}}(\theta_{\perp\mathbf{k}})$ of Eq. (17), have to be taken in the direction $\theta_{\perp\mathbf{k}}$ perpendicular to $\mathbf{k}$. The fast ϵ_k^3 decrease (as $\epsilon_k\to0$) is due to the vertex renormalization, since $\varepsilon_{\rm RPA}$ in Eq. (37) diverges for $q\ll k_{\rm TF}$ [see Eq. (12)].

Hereafter we remove the subindex $\perp$ from the anisotropic parameters in those expressions where they are assumed to be angle-independent or only their order of magnitude matters.

2. Zero temperature, larger k

For $\epsilon_k \gg \hbar v_s k_{\rm TF}$ we obtain the result

$$-\,\mathrm{Im}\,\Sigma_+^{\rm PA}(k,\epsilon_k) \simeq \frac{\lambda}{4}\hbar v_s k \int_0^1 \frac{y^2\sqrt{1-y^2}}{\left(y+\frac{k_{\rm TF}}{2k}\right)^2}\,dy = \frac{\lambda\hbar v_s k}{4} f\left(\frac{k_{\rm TF}}{2k}\right), \tag{42}$$

$$f(x) = 3x + \frac{\pi}{4}(1-6x^2) + \frac{(3x^3-2x)\,\mathrm{acosh}(x^{-1})}{\sqrt{1-x^2}}. \tag{43}$$

This admits two regimes: for $\hbar v_s k_{\rm TF} \ll \epsilon_k \ll E_F$,

$$-\mathrm{Im}\,\Sigma_+^{\rm PA}(k,\epsilon_k) \simeq \frac{\lambda k_B T_{\rm BG}}{8} f\left(\frac{2\alpha_{\rm fs}}{\bar{\varepsilon}_0}\right), \tag{44}$$

while for $\epsilon_k \gg E_F$ we obtain

$$-\mathrm{Im}\,\Sigma_+^{\rm PA}(k,\epsilon_k) \simeq \frac{\pi\lambda v_s}{16 v_F}\epsilon_k. \tag{45}$$

Returning to the low-energy ($\epsilon_k \ll \hbar v_s k_{\rm TF}$) regime [see Eq. (41)], we note that, without the vertex screening effect [that is, setting $\varepsilon_{\rm RPA} \to 1$ in Eq. (37)], instead of the ϵ_k^3 behavior one would find the linear ϵ_k dependence characteristic of a marginal Fermi liquid,

$$-\mathrm{Im}\,\Sigma^{\rm PA}_{+(\text{no scr})}(\mathbf{k},\epsilon_k) \simeq \frac{\lambda_\perp}{8}\epsilon_k, \tag{46}$$

which (for materials such that $k_{\rm TF} \ll k_F$) behaves similarly to the true self-energy in the range $\hbar v_s k_{\rm TF} \ll \epsilon_k \ll \hbar v_s k_F$, since $\varepsilon_{\rm RPA}$ tends to unity for the momenta $q \gg k_{\rm TF}$ dominating the integral (37). We will see, however, that a small offset remains due to the contribution of the screened low-q values ($q \ll k_{\rm TF}$).

Table I shows representative angle-independent material parameters, including those that will be used for the numerical calculations discussed in Sec. V. From Eqs. (41), (46), and the parameter values shown in Table I, it is safe to conclude that, at zero temperature, the damping rate due to electron-phonon coupling is always much smaller than ϵ_k. Thus the single-electron quasiparticles near the Fermi surface are well defined.

3. Small k, low nonzero temperature

So far we have assumed zero temperature, i.e., $k_B T \ll \epsilon_k$. At nonzero temperatures, the vertex renormalization is fundamental to avoid logarithmic divergences. These occur for the unscreened self-energy at any nonzero temperature due to the divergent contribution of small-q values. Focusing on the correctly screened self-energy, we consider first the nonzero, low-temperature limit $\epsilon_k \ll k_B T \ll 2\hbar v_s k_{\rm TF}, k_B T_{\rm BG}$. Again, only the perpendicular-to-**k** substrate-related constants appear. We obtain

$$-\,\mathrm{Im}\,\Sigma_+^{\rm PA}(k,\epsilon_k) \simeq \lambda_\perp k_B T \left(\frac{k_F}{k_{\rm TF\perp}}\right)^2 \left(\frac{T}{T_{\rm BG\perp}}\right)^2 \frac{7\zeta(3)}{2}, \tag{47}$$

with $7\zeta(3)/2 \simeq 4.21$. The essential independence from k of the lifetime (which allows for the replacement $k \simeq k_F$) is a general property of the case $\epsilon_k \ll T$. In those materials where ε_0 is so high that $k_{\rm TF} \ll k_F$ and therefore a temperature regime exists such that $\epsilon_k \ll \hbar v_s k_{\rm TF} \ll k_B T \ll k_B T_{\rm BG}$, the T^3 law is replaced by a $\sim T \log T$ behavior. Specifically, the asymptotic expression reads

$$-\mathrm{Im}\,\Sigma_+^{\rm PA}(k,\epsilon_k) \simeq \lambda_\perp k_B T \left(\frac{k_F}{k_{\rm TF\perp}}\right)^2 \log\left(\frac{\hbar v_s k_{\rm TF}}{k_B T}\right). \tag{48}$$

4. Small k, high temperature

The high-temperature limit ($T_{\rm BG} \ll T$, while only $\epsilon_k \ll E_F$ is required), where phonons are nondegenerate, yields

$$-\mathrm{Im}\,\Sigma_+^{\rm PA}(k,\epsilon_k) \simeq \frac{\lambda}{4}k_B T \int_0^1 \frac{y\sqrt{1-y^2}}{\left(y+\frac{k_{\rm TF}}{2k}\right)^2}\,dy = \frac{\lambda k_B T}{4} g\left(\frac{k_{\rm TF}}{2k}\right), \tag{49}$$

$$g(x) = -2 + \pi x + \frac{(1-2x^2)\,\mathrm{acosh}(x^{-1})}{\sqrt{1-x^2}}. \tag{50}$$

The logarithmic divergence of the function g at $x \to 0$ becomes relevant in the limit $k \gg k_{\rm TF}$, where

$$-\mathrm{Im}\,\Sigma_+^{\rm PA}(k,\epsilon_k) \simeq \frac{\lambda k_B T}{4}\left[\log\left(\frac{4k}{k_{\rm TF}}\right) - 2\right]. \tag{51}$$

5. Comparison with graphene intrinsic phonons

Comparing Eqs. (41), (47), and (49) with the corresponding limiting expressions for the electron self-energy induced by the graphene-intrinsic deformation-potential acoustic (DA) phonons [26], we see below that, for an important range of parameter values, the inverse lifetime is dominated by the piezoelectric substrate phonons.

For our estimates we borrow $\Sigma_+^{\rm DA}(k,\epsilon_k)$ from Ref. [26]. Specifically, with a deformation constant $D \simeq 25$ eV, and taking $k_F = [k_F]\,10^6\,\mathrm{cm}^{-1}$ (this momentum unit corresponds to a density of $k_F^2/\pi \simeq 3.2 \times 10^{11}\ \mathrm{cm}^{-2}$), one obtains from (41)

$$\frac{\mathrm{Im}\,\Sigma_+^{\rm PA}(k,\epsilon_k)}{\mathrm{Im}\,\Sigma_+^{\rm DA}(k,\epsilon_k)} \simeq \frac{20}{[k_F]^2}\lambda\bar{\varepsilon}_0^2\frac{\epsilon_k}{1\ \mathrm{meV}} \tag{52}$$

for $k_B T \ll \epsilon_k \ll \hbar v_s k_{\rm TF}$.

Likewise, at nonzero temperatures ($\epsilon_k/k_B \ll T \ll T_{\rm BG}$), we have from (47)

$$\frac{\mathrm{Im}\,\Sigma_+^{\rm PA}(k,\epsilon_k)}{\mathrm{Im}\,\Sigma_+^{\rm DA}(k,\epsilon_k)} \simeq \frac{100}{[k_F]^2}\lambda\bar{\varepsilon}_0^2\frac{k_B T}{1\ \mathrm{meV}}. \tag{53}$$

Finally, at high temperatures ($\epsilon_k/k_B \ll T_{\rm BG} \ll T$), one obtains from (49) the k-independent ratio

$$\frac{\mathrm{Im}\,\Sigma_+^{\rm PA}(k,\epsilon_k)}{\mathrm{Im}\,\Sigma_+^{\rm DA}(k,\epsilon_k)} \simeq \frac{35\,g\left(\frac{2\alpha_{\rm fs}}{\bar{\varepsilon}_0}\right)}{[k_F]}\lambda. \tag{54}$$

From these ratios we conclude that piezoelectric acoustic phonons can dominate over deformation acoustic phonons in an appreciable range of realistic material parameters, especially for small carrier concentrations. The smaller value of $D \simeq 6.8$ eV also found in the literature [42,43] would further increase the relative importance of piezoelectric phonons against intrinsic ones.

C. Real part: Anisotropic Fermi velocity

For the real part of the self-energy, we have, from Eq. (33),

$$\mathrm{Re}\,\Sigma_+^{\mathrm{PA}}(\mathbf{k},\omega) = \sum_{s=\pm}\int \frac{d\mathbf{q}}{(2\pi)^2}\left|\frac{\gamma_{\mathbf{q}}^{\mathrm{PA}}}{\varepsilon_{\mathrm{RPA}}(\mathbf{q},0)}\right|^2 F_{+s}(\mathbf{k},\mathbf{k}') \times\left[\frac{n_B(\hbar\omega_{\mathbf{q}})+n_F(\epsilon_{k's})}{\hbar\omega+\hbar\omega_{\mathbf{q}}-\epsilon_{k's}} + \frac{n_B(\hbar\omega_{\mathbf{q}})+1-n_F(\epsilon_{k's})}{\hbar\omega-\hbar\omega_{\mathbf{q}}-\epsilon_{k's}}\right], \tag{55}$$

where the denominators are to be understood as principal values. Unlike for many-body effects directly caused by the electron-electron interaction, this phonon contribution to the electron self-energy tends to be negligibly small compared to the Fermi energy. However, its derivatives are large. As a result, the phonon-induced contributions to the Fermi velocity renormalization are larger than those stemming from the direct electron-electron interactions.

Since $\partial\,\mathrm{Re}\,\Sigma_+^{\mathrm{PA}}(\mathbf{k},\omega)/\partial(v_F\mathbf{k})$ is, by a factor of v_s/v_F, smaller than $\partial\,\mathrm{Re}\,\Sigma_+^{\mathrm{PA}}(\mathbf{k},\omega)/\partial\omega$ (see Ref. [44]), it suffices to focus on the frequency derivative, in contrast to the case of electron-electron interactions, where both derivatives matter [27,45]. We thus approximate

$$\tilde{v}_F(\hat{\mathbf{k}}) = v_F\left[1-\left.\frac{\partial\,\mathrm{Re}\,\Sigma_+^{\mathrm{PA}}(\hat{\mathbf{k}}k_F,\omega)}{\partial\omega}\right|_{\omega=0}\right]^{-1} \tag{56}$$

for the (direction-dependent) renormalization of the Fermi velocity in graphene induced by piezoelectric acoustic substrate phonons.

For further analysis, it us useful to separate Eq. (33) into three terms,

$$\Sigma_+^{\mathrm{PA}} = \Sigma_+^{(\mathrm{ph})} + \Sigma_+^{(\mathrm{el})} + \Sigma_+^{(\mathrm{vac})}, \tag{57}$$

where $\Sigma_+^{(\mathrm{ph})}$ contains just the Bose factor $n_B(\hbar\omega_{\mathbf{q}})$, $\Sigma_+^{(\mathrm{el})}$ contains the Fermi factor $n_F(\epsilon_{k's})$, and $\Sigma_+^{(\mathrm{vac})}$ contains the remaining vacuum term. As in the previous subsection, angle-independent material parameters are assumed in the following.

The real part of $\Sigma_+^{(\mathrm{vac})}$ at $\omega=0$ is independent of the Fermi energy:

$$\mathrm{Re}\,\Sigma_+^{(\mathrm{vac})}(k,0) \simeq -\frac{\lambda}{16}\frac{v_s}{v_F}\left[\hbar v_F k_c + \hbar v_F k\log\left(\frac{k_c-k}{k}\right)\right], \tag{58}$$

where k_c is a cutoff momentum of the order of the inverse lattice spacing. Because of the small prefactor, $\mathrm{Re}\,\Sigma_+^{(\mathrm{vac})}(k_F,0)$ represents a weak correction to the chemical potential for all relevant carrier densities, even for $k_c \gg k_F$. We will see that its derivative can also be neglected because $\partial_\omega \mathrm{Re}\,\Sigma_+^{(\mathrm{vac})}(k_F,0) \simeq (\lambda/4)(v_s/v_F)(1+\log k_F/k_c) \ll \partial_\omega \mathrm{Re}\,\Sigma_+^{(\mathrm{el})}(k_F,0)$.

At temperatures $T \ll T_{\mathrm{BG}}$, the term containing the Bose factors $\mathrm{Re}\,\Sigma_+^{(\mathrm{ph})}$ is exponentially small, while at temperatures $T \gg T_{\mathrm{BG}}$ it does not grow larger than a factor T/T_{BG} times the expression in Eq. (58). Hence we can also neglect $\partial_\omega \mathrm{Re}\,\Sigma_+^{(\mathrm{ph})}$.

Thus the only term that can affect the electronic properties is $\mathrm{Re}\,\Sigma_+^{(\mathrm{el})}(\mathbf{k},\omega)$, which is likewise small in magnitude, at most twice the term shown in Eq. (58), but it has a large derivative. Note that here the quasielastic approximation ($\hbar\omega_{\mathbf{q}} \ll \epsilon_{k'}$) is not informative, since $\mathrm{Re}\,\Sigma_+^{(\mathrm{el})}(\mathbf{k},\omega)$ vanishes when $\hbar\omega_{\mathbf{q}}$ is set to zero.

The integral

$$\left.\frac{\partial\,\mathrm{Re}\,\Sigma_+^{(\mathrm{el})}(\hat{\mathbf{k}}k_F,\omega)}{\partial\omega}\right|_{\omega=0} = -\sum_{s=\pm}\int\frac{d\mathbf{q}}{(2\pi)^2}\left|\frac{\gamma_{\mathbf{q}}^{\mathrm{PA}}}{\varepsilon_{\mathrm{RPA}}}\right|^2 F_{+s}(\mathbf{k},\mathbf{k}') \times n_F(\epsilon_{k's})\left[\frac{1}{(\epsilon_{k's}-\hbar\omega_{\mathbf{q}})^2}-\frac{1}{(\epsilon_{k's}+\hbar\omega_{\mathbf{q}})^2}\right] \tag{59}$$

can be computed by changing variables ($d\mathbf{q} \to d\mathbf{k}'$, with $\mathbf{k}' = \mathbf{k}+\mathbf{q}$) and performing the radial integral first by parts, with

$$u = k' n_F(\epsilon_{k's}), \quad dv = \frac{dk'}{(\epsilon_{k's} \pm \hbar v_s q)^2}.$$

We arrive at a direction-dependent expression that integrates over the Fermi surface:

$$\left.\frac{\partial\,\mathrm{Re}\,\Sigma_+^{(\mathrm{el})}(\hat{\mathbf{k}}k_F,\omega)}{\partial\omega}\right|_{\omega=0} = -\int_0^{2\pi}\frac{d\alpha}{\hbar v_F(2\pi)^2}\left|\frac{\gamma_{\mathbf{k}+\mathbf{q}}^{\mathrm{PA}}}{\varepsilon_{\mathrm{RPA}}}\right|^2 \times F_{+s}(\mathbf{k},\mathbf{k}+\mathbf{q})\frac{2}{\hbar\omega_{\mathbf{q}}}, \tag{60}$$

where, as in (29), α is the angle between $\mathbf{k}$ and $\mathbf{k}+\mathbf{q}$.

After further averaging over the Fermi surface ($\hat{\mathbf{k}}$ directions), the ratio (56) becomes similar to the temperature prefactor of the high-temperature damping (49),

$$\tilde{v}_F = \frac{v_F}{1+\frac{\lambda}{4\pi}f\left(\frac{k_{\mathrm{TF}}}{2k_F}\right)}, \tag{61}$$

where, we recall, all variables are angle-averaged. Inspection of Eq. (61) shows that the renormalization of the Fermi velocity cannot exceed 3% even for $K_R^2 \sim 1$, and K_R is usually much smaller. The result shown in Eq. (61) permits us to confirm the validity of neglecting the vacuum and phonon self-energy parts. A more accurate estimate of the ratios between derivatives yields $\partial_\omega \mathrm{Re}\,\Sigma_+^{(\mathrm{vac})}/\partial_\omega \mathrm{Re}\,\Sigma_+^{(\mathrm{el})} = O(v_s/v_F) \ll 1$, while $\partial_\omega \mathrm{Re}\,\Sigma_+^{(\mathrm{ph})}/\partial_\omega \mathrm{Re}\,\Sigma_+^{(\mathrm{el})}$ is $O(v_s/v_F)$ for $T \ll T_{\mathrm{BG}}$ and $O(T/T_F)$ for $T_{\mathrm{BG}} \ll T \ll T_F$.

D. Electron mobility

1. *Transport lifetime*

Within Boltzmann transport theory, the momentum (or transport) relaxation time $\tau_{+\mathrm{tr}}(\mathbf{k})$ (where the subscript denotes "transport" and + denotes the band) is calculated analogously to the inverse lifetime in Sec. IV B, but with an extra angular factor $(1-\cos\alpha) = q^2/2k^2$ in the integrand, which increases the weight of large-angle scattering processes. Specifically, Eq. (37) is replaced by

$$\frac{\hbar}{2\,\tau_{+\mathrm{tr}}^{\mathrm{PA}}(\mathbf{k})} = \pi\sum_{s=\pm}\sum_{t=\pm}\int\frac{d\mathbf{q}}{(2\pi)^2}\frac{q^2}{2k^2}\left|\frac{\gamma_{\mathbf{q}}^{\mathrm{PA}}}{\varepsilon_{\mathrm{RPA}}(\mathbf{q},0)}\right|^2\frac{1+s\cos\alpha}{2} \times [n_F(\hbar\omega_{\mathbf{q}}+t\epsilon_k)+n_B(\hbar\omega_{\mathbf{q}})]\delta(\epsilon_{k+}-\epsilon_{k's}), \tag{62}$$

where the quasielastic approximation has been made. The inclusion of this additional q^2 factor in the integrand improves the quasielastic approximation, changes the power-law scaling at low temperatures (by generating an extra factor T^2), and corrects the lifetime with a constant factor at temperatures greater than $T_{\rm BG}$.

2. Low temperature

For quasiparticle energies such that ($\epsilon_k/k_B \ll T$), we find (after angle averaging) results that are essentially independent of ϵ_k, i.e., $\tau^{\rm PA}_{+\rm tr}(k) \simeq \tau^{\rm PA}_{+\rm tr}(k_F)$. In the low, yet nonzero, temperature regime $\epsilon_k/k_B \ll T \ll 2r_s T_{\rm BG}$, we obtain

$$\frac{\hbar}{2\,\tau^{\rm PA}_{+\rm tr}(k_F)} \simeq \frac{\lambda k_B T}{8}\left(\frac{k_B T}{\hbar v_s k_{\rm TF}}\right)^4 \frac{k_{\rm TF}^2}{k_F^2}\int_0^\infty dx\, x^4 \mathrm{csch}(x) = \frac{\lambda k_B T}{8}\left(\frac{\bar{\varepsilon}_0}{\alpha_{\rm fs}}\right)^2\left(\frac{T}{T_{\rm BG}}\right)^4 \frac{93\zeta(5)}{2} \tag{63}$$

[$93\zeta(5)/2 \simeq 48.2$], which should be compared to Eq. (47). The shift from T^3 to T^5 behavior is due to the transport-induced reduced weight (by a factor $q^2/2k_F^2$) of the low-q values dominating the inverse transport lifetime at low temperatures.

If the vertex screening is neglected, we still obtain a convergent result, despite the temperature being nonzero, because the low-q divergence is already suppressed by the transport-associated angular weighting factor. We obtain

$$\frac{\hbar}{2\,\tau^{\rm PA}_{+\rm tr}(k_F)_{(\rm no\ scr)}} \simeq \frac{\lambda 7\zeta(3)}{4} k_B T\left(\frac{T}{T_{\rm BG}}\right)^2, \tag{64}$$

and we recall that the nontransport equivalent of this equation is divergent, as discussed in Sec. IV B [see discussion before (47)]. The limit (64) is coincident with the T^3 dependence found in Ref. [43], where vertex screening in the particular case of GaAs is not taken into account. The neglect of vertex screening is acceptable in the temperature regime $2r_s T_{\rm BG} \lesssim T \ll T_{\rm BG}$ in those materials with $4r_s \ll 1$, because in that case the integral in Eq. (62) is dominated by exchanged momenta q such that $k_{\rm TF} \ll q \ll k_F$, which are a little bit sensitive to vertex screening. This intermediate regime of temperatures does not exist for substrate materials such that $2r_s \sim 1$.

3. High temperature

For the high-temperature range $T \gg T_{\rm BG}$, we have

$$\frac{\hbar}{2\,\tau^{\rm PA}_{+\rm tr}(k_F)} \simeq \frac{\lambda}{2} k_B T\int_0^1 x\sqrt{1-x^2}\,dx = \frac{\lambda}{6} k_B T, \tag{65}$$

to be compared with Eq. (49). The absence of a qualitative change in the temperature dependence as we shift from nontransport to transport lifetime is due to the relatively small weight, at high temperatures, of the transport-reduced, low-q processes.

Thus we see that the transport scattering rates are comparable to the previous imaginary self-energies except for an extra $(T/T_{\rm BG})^2$ factor appearing at low temperatures due to extra angular suppression of the otherwise dominant low-q events. A similar comparison holds for the intrinsic acoustic deformation-potential phonons, where

$$\frac{\hbar}{2}\tau^{\rm DA}_{+\rm tr}(k_F)^{-1} \simeq 10\left(\frac{T}{T_{\rm BG}}\right)^2 \mathrm{Im}\,\Sigma^{\rm DA}_+(k_F,0) \tag{66}$$

at low temperatures, while

$$\frac{\hbar}{2}\tau^{\rm DA}_{+\rm tr}(k_F)^{-1} \simeq \frac{1}{2}\,\mathrm{Im}\,\Sigma^{\rm DA}_+(k_F,0) \tag{67}$$

for high temperatures. In the last two equations, we are comparing the results of Refs. [43] and [26] for the transport scattering rate and the inverse lifetime, respectively.

4. Comparison with graphene intrinsic phonons

In analogy with Sec. IV B, we may compare the transport rates due to deformation and piezoelectric phononic modes. In the low-temperature limit (as before, $[k_F]$ is k_F in units of $10^6\,\mathrm{cm}^{-1}$),

$$\frac{\tau^{\rm PA}_{+\rm tr}(k_F)^{-1}}{\tau^{\rm DA}_{+\rm tr}(k_F)^{-1}} \simeq \frac{200}{[k_F]^2}\lambda\bar{\varepsilon}_0^2\frac{k_B T}{1\ \mathrm{meV}}, \tag{68}$$

while at temperatures above $T_{\rm BG}$,

$$\frac{\tau^{\rm PA}_{+\rm tr}(k_F)^{-1}}{\tau^{\rm DA}_{+\rm tr}(k_F)^{-1}} \simeq \frac{45}{[k_F]}\lambda, \tag{69}$$

independent of temperature. Upon inserting the specific material parameters, Eq. (69) is in agreement with the calculations of Ref. [43], where PA and DA transport rates are compared for GaAs. Equations (68) and (69) must be compared to Eqs. (53) and (54) of Sec. IV B, respectively. As in the nontransport lifetime estimates presented therein, we note that piezoelectric phonons dominate over deformation phonons at nonsmall couplings and low densities. We recall that Ref. [43] used a deformation constant $D = 6.8$ eV, quite smaller than the value $D = 25$ eV [26] we have used here. That replacement reduces $1/\tau^{\rm DA}$ by about a factor of 10 and makes the substrate PA phonons relatively more important.

5. Mobility

Finally, in order to compute the electron mobility, we average the momentum relaxation time [see Eq. (62)],

$$\overline{\tau_{\rm tr}} \equiv \int d\epsilon\, D(\epsilon)\tau_{+\rm tr}(k(\epsilon))[-dn_F(\epsilon)/d\epsilon], \tag{70}$$

and because the energy derivative peaks at E_F while $\tau_{+\rm tr}(k)$ varies slowly with k, one can write the classical Drude formula for the mobility,

$$\mu = \frac{e\,\tau_{+\rm tr}(k_F)}{m^*}, \tag{71}$$

in terms of $\tau_{+\rm tr}(k)$ computed at the Fermi level and the "effective mass" $m^* = \hbar k_F/v_F$ of the graphene Dirac fermions.

V. NUMERICAL RESULTS

In the following, we present and discuss numerical results for the various rates and mean free paths derived in Secs. IV B and IV D. Unless otherwise stated, the numerical values of this section are computed for ZnO substrates (Z cut), which are isotropic (see Fig. 2) and whose parameters are $\lambda = 0.03$

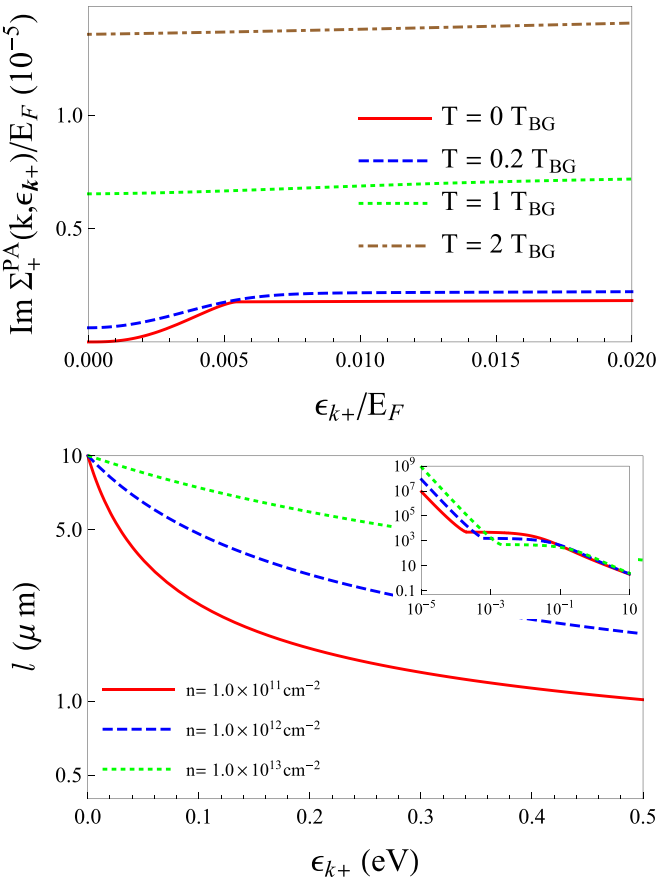

FIG. 4. Imaginary part of the self-energy and inelastic-scattering length of charge carriers in graphene on ZnO (Z cut) as a function of the energy, $\epsilon_k/E_F = (k - k_F)/k_F$. Upper: Im Σ_+^{PA} for different temperatures. The curves are valid for all densities. Lower: inelastic mean free path l for different carrier concentrations at room temperature ($T = 300$ K $= 26$ meV$/k_B$). The inset shows l at $T = 0$ for the same densities. The Bloch-Grüneisen temperature T_{BG} is given in Eq. (40). For this material, $k_B T_{BG} = 0.0054 E_F$ (for all carrier densities) and $k_{TF}/k_F \simeq 2$ (thus $T_{BG} \simeq \hbar v_s k_{TF}/k_B$). For these three densities, $k_B T_{BG} = 0.2$, 0.63, and 2 meV, while $E_F = 37.4$, 117, and 374 meV.

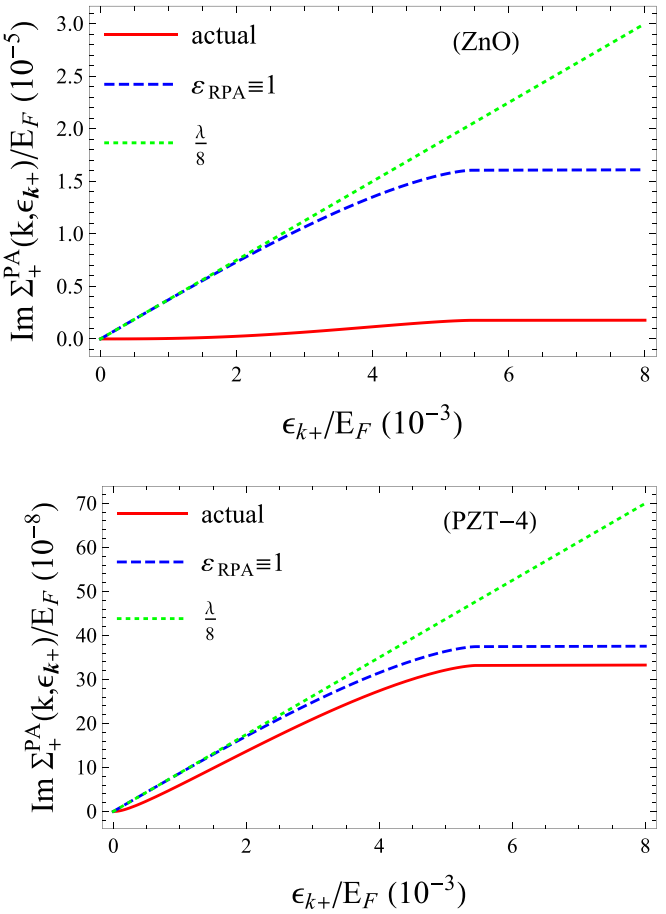

FIG. 5. Low-energy behavior of the imaginary part of the self-energy at zero temperature. The solid, dashed, and dotted lines correspond, respectively, to the exact values, the values without vertex screening, and the values obtained (in the unscreened case) from the linear $\lambda/8$ approximation of Eq. (46). Upper: graphene on ZnO (Z cut). Lower: graphene on PZT-4 (Z cut), for which $k_B T_{BG}/E_F = 0.0045$, $k_{TF}/k_F \simeq 0.025$, and $\hbar v_s k_{TF}/E_F \simeq 5.7 \times 10^{-5}$. See Table I for λ values.

and $\bar{\varepsilon}_0 = 4.8$, which implies $k_{TF}/k_F \simeq 2$ and $k_B T_{BG}/E_F \simeq 0.0054$. Estimates for other substrate material parameters can be readily obtained from inspection of the various analytical limiting expressions derived in the previous section.

A. Imaginary part

In the upper plot of Fig. 4, we show the imaginary part of the on-shell self-energy as a function of the parameter $\epsilon_k/E_F > 0$ for different temperatures. The curves are universal in the sense that they are density-independent. The zero-temperature curve shows, for small ϵ_k, the limiting ϵ_k^3 behavior of Eq. (41), which arises due to the combined effect of screening and the phase-space restrictions faced by the electrons when losing energy via phonon emission. This restriction disappears when ϵ_k is greater than any phononic energy, i.e., $\epsilon_k \gg k_B T_{BG}$. Above this threshold, the imaginary part of the self-energy becomes energy-independent, as predicted by Eq. (44). At still higher energies ($\epsilon_k \gg E_F$, not shown in the upper plot of Fig. 4), it increases linearly with the length of the constant energy circumference at the quasiparticle energy $E_{k+} \propto k$. Such a linear increase with k would appear with a negligible slope in the tiny scale of $\epsilon_k \propto (k - k_F)$ of the upper plot of Fig. 4. Specifically, the slope is, in the dimensionless units of the upper plot of Fig. 4, $(\lambda\pi/16)(v_s/v_F)$.

The upper plot of Fig. 4 also shows that a further increase in temperature ($T > T_{BG}$) smears these features due to phonon excitation and electron heating near the Fermi energy, as exemplified in Eq. (49). The effect of vertex screening in the regime of low ϵ_k and low T can be appreciated in Fig. 5 for both ZnO and (angle-averaged) PZT substrates with its higher dielectric constant (and thus smaller λ). For the sake of comparison, the graphics include also the linear approximation (46), which holds better for PZT because its large dielectric constant reduces the size of the phase-space region where the screening of the phonon interaction by the electron cloud (vertex correction) is really important. Unlike for ZnO, in this material k_{TF} is considerably smaller than k_F,

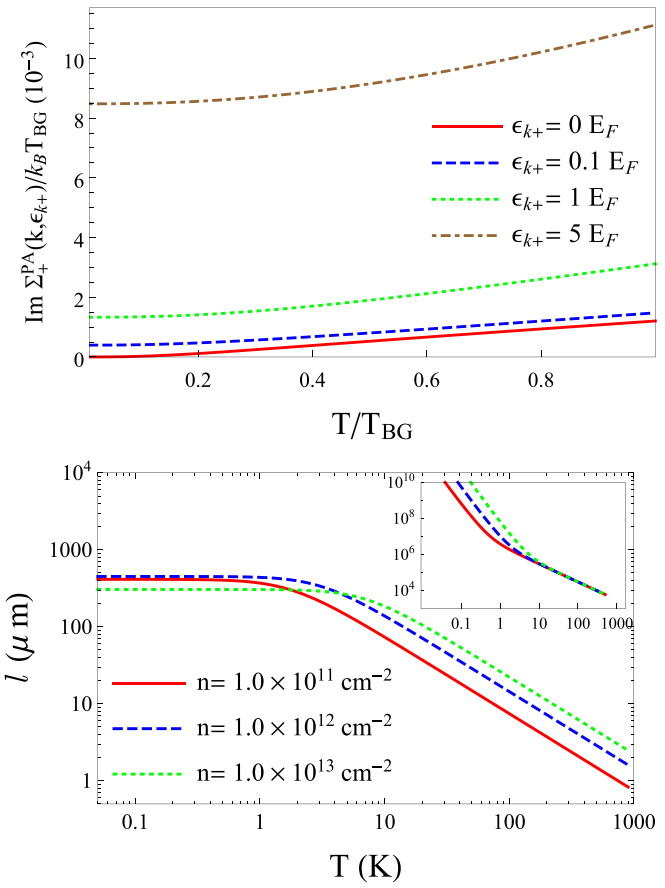

FIG. 6. Imaginary part of the self-energy and inelastic-scattering length. Upper: Im Σ_+^{PA} as a function of T/T_{BG} for different values of ϵ_k/E_F. Lower: l as a function of T for $\epsilon_k = 0.1$ eV $\simeq 1160$ K and different doping levels. The inset shows the corresponding curves for $\epsilon_k = 0$. Here, $E_F \simeq 185 k_B T_{BG}$. The values of T_{BG} for these three densities are 2.35, 7.35, and 23.5 K.

which leaves room for an intermediate range of ϵ_k values for which the approximation $\varepsilon_{RPA} \simeq 1$ is acceptable while the linear behavior still holds. As announced in Sec. IV B, after Eq. (46), there is an offset between the true imaginary self-energy and the linear approximation due to the reduced contribution of the screened low-q processes.

The upper plot of Fig. 6 shows the temperature dependence of Im Σ_+^{PA} for fixed values of ϵ_k. At low temperatures ($T \ll \epsilon_k$, hot electron regime), these decay linewidths are independent of T. Note that in this figure the nonzero values of ϵ_k are well above $\hbar v_s k_{TF}$ and thus the limit (41) does not apply. At higher temperatures ($T > T_{BG}$), the linear behavior of Eq. (49) is recovered.

B. Inelastic mean free path

The lower plots of Figs. 4 and 6 are devoted to the inelastic-scattering mean free path, which is the inverse of the imaginary part of the on-shell self-energy:

$$l(k) = \frac{\hbar v_F}{2\,\mathrm{Im}\,\Sigma_+^{PA}(k,\epsilon_k)}. \tag{72}$$

The lower plot of Fig. 4 shows values for $l(k)$ as a function of ϵ_k for three cases of typical doping conditions. Note that they tend to coincide at small ϵ_k, as suggested by Eq. (49) (case $T > T_{BG}$), which predicts a doping-independent low-ϵ_k ($k \to k_F$) limit at nonzero temperatures. Finally, the inset of the lower plot of Fig. 4 clearly displays the three energy regimes that hold at zero temperature and which can be inferred from Eqs. (41)–(45).

The temperature dependence of l is shown in the lower plot of Fig. 6. A crossover from (T-independent) low-temperature to (T^{-1}) high-temperature behavior can be appreciated for $T \sim T_{BG}$, in agreement with Eqs. (41) and (49). One must note, however, that Eq. (41) does not truly apply to the low-temperature sector of this graph, because here $\epsilon_k > \hbar v_s k_{TF}$, unlike the assumption in (41). This explains the discrepancy in the density dependence. For this material, $\hbar v_s k_{TF}$ takes values 0.2, 0.63, and 2 meV for the three listed densities, all much smaller than the value $\epsilon_k = 100$ meV considered there.

The inset shows the corresponding curves for $\epsilon_k = 0$. A clear crossover for T^{-3} to T^{-1} behavior is observed at $T \sim T_{BG}$, in agreement with Eqs. (47) and (49).

C. Density dependence

For a fixed value of k and at room temperature, Fig. 7 shows the variation of Im Σ_+^{PA} and of the mean free path as a

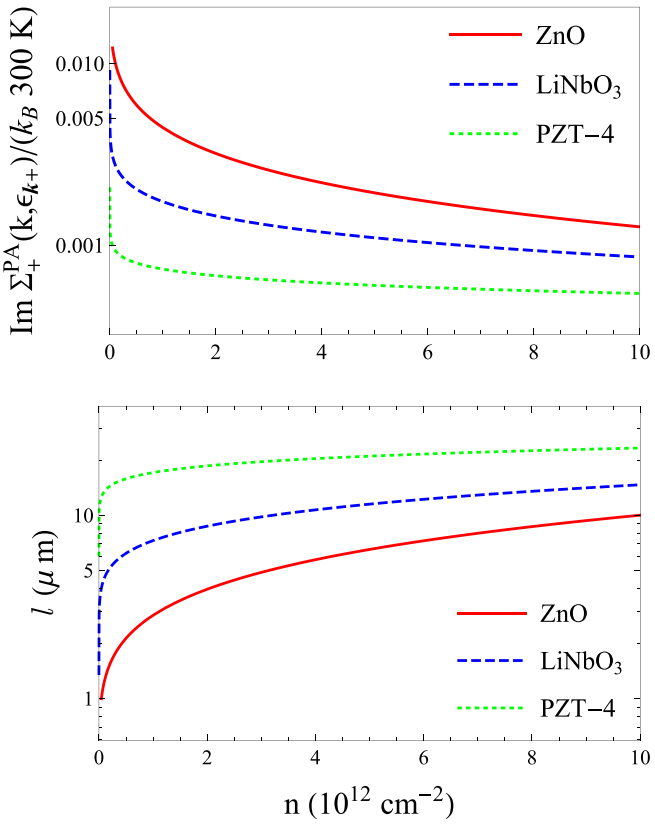

FIG. 7. Imaginary part of the self-energy and inelastic-scattering length as a function of doping, for different materials, at fixed (room) temperature and electronic state $k = \sqrt{\pi \times 10^{13}}$ cm^{-2} (recall $k_F = \sqrt{\pi n}$). Upper: Im Σ_+^{PA} as a function of carrier density n. Lower: l as a function of n in the same units for the same materials.

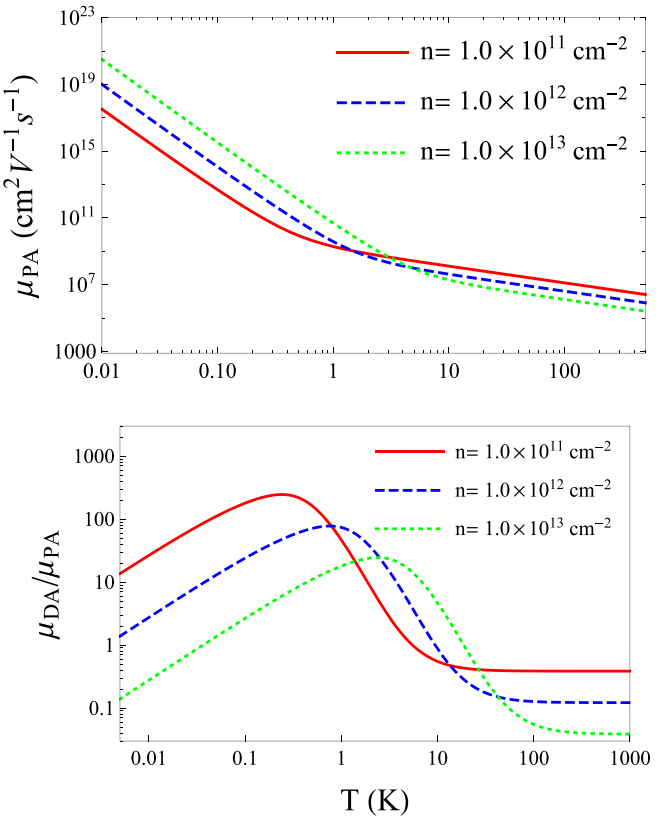

FIG. 8. Electron mobility due only to piezoelectric acoustic phonons and its comparison with that due to intrinsic phonons. Upper: the mobility μ_{PA} as a function of the temperature, for several carrier concentrations. Lower: the ratio μ_{DA}/μ_{PA}, where μ_{DA} is the mobility obtained when only the deformation potential of intrinsic phonons (with $D = 25$ eV) is included. The ratio between mobilities must be increased by a factor $(25/6.8)^2 \simeq 13.5$ when the value $D = 6.8$ eV is used [43]. The values of T_{BG} for these doping levels are given in the caption of Fig. 6, while $T_F = 434$, 1360, and 4340 K.

function of the carrier density. A logarithmic divergence in the linewidth, accompanied by a vanishing mean free path, is seen to appear in the undoped regime, where the description of the system employed in the present paper is not valid anymore. This spurious low-doping behavior can be expected from an extrapolation of Eq. (49) to low doping.

D. Mobility: Comparison with intrinsic phonons

In the upper plot of Fig. 8, we show the electron mobility μ [see Eq. (71)] due only to piezoelectric phonons. The T^{-5} and T^{-1} behaviors can be appreciated at low and high temperatures, respectively, as expected from Eqs. (63) and (65), taking into account Eq. (71) for the density dependence.

Finally, in the lower plot of Fig. 8 we compare the substrate-induced mobility to that stemming only from graphene intrinsic phonons, with $D = 25$ eV. The total combined mobility due to (piezoelectric and intrinsic deformation) acoustic phonons is $\mu = (\mu_{PA}^{-1} + \mu_{DA}^{-1})^{-1}$. Specifically, we plot the ratio between the two inverse mobilities. The smaller value of $D = 6.8$ eV reduces the intrinsic inverse mobility by an order of magnitude and correspondingly increases the relative importance of piezoelectric phonons. This ratio between transport scattering rates shows two clear low- and high-T regimes with linear-in-T and T-independent behaviors, respectively, in agreement with Eqs. (68) and (69). At low and high temperatures, the relative importance of the PA phonons increases with decreasing density. There is an intermediate temperature regime in which the density dependence is inverted. Thus we see that the piezoelectric phonons dominate over a wide range of temperatures and densities. If $D = 6.8$ eV is chosen for the intrinsic phonons, then the momentum relaxation due to PA phonons computed here prevails essentially always except at very high temperature and density or for extremely low temperatures.

VI. CONCLUSIONS

We have studied the effective interaction of charge carriers in graphene on a piezoelectric substrate, as modified by the acoustic phonons of the piezoelectric substrate. Our diagrammatic approach takes into account the renormalization of both phonon modes and carrier states due to the mutual interaction, and it emphasizes the importance of all the involved screening processes for a correct evaluation of the mean free path and carrier mobility. We have obtained numerous analytical limits as a function of carrier energy, density, and temperature, which have allowed us to understand the trends shown by the numerical results.

We may emphasize that the inverse mobility due to piezoelectric acoustic phonons increases with carrier density at high temperatures while it is a decreasing function of density at low temperatures (see the upper plot in Fig. 8), the latter trend being understandable in terms of increased electron screening at high densities. On the other hand, the temperature dependence of the inverse mobility is much more pronounced at low temperatures.

When compared with the values obtained when only intrinsic deformation phonons are taken into account, we find that the contributions of the piezoelectric acoustic phonons to the inverse lifetime and mobility dominate over a considerable range of temperatures and doping levels, a parameter range that becomes almost pervasive if low values of the deformation coupling constant are chosen from the literature.

As our results are applicable to piezoelectric materials of various lattice symmetries and interaction strengths, they will be helpful in the development of electronic devices involving graphene deposited on piezoelectric substrates. Among such potential devices, we may mention the graphene field-effect transistor on a piezoelectric substrate as studied experimentally in Refs. [24] and [25] with PZT and $LiNbO_3$, respectively. That class of setups was also investigated as a possible basis for the building of nonvolatile memories [46]. Finally, a suitable understanding of the interaction between graphene electrons and acoustic piezoelectric phonons will enhance applications based on the use of piezoelectric surface acoustic waves beneath a graphene layer.

ACKNOWLEDGMENTS

We wish to thank Fernando Calle and Jorge Pedrós for valuable discussions. This work has been supported by

Spain's MINECO through Grants No. FIS2011-23713 and No. FIS2013-41716-P; the European Research Council Advanced Grant (Contract No. 290846), and the European Commission under the Graphene Flagship, Contract No. CNECTICT-604391. D.G.G. acknowledges financial support from Campus de Excelencia Internacional (Campus Moncloa UCM-UPM).

[1] R. Weigel, D. Morgan, J. Owens, A. Ballato, K. Lakin, K.-Y. Hashimoto, and C. Ruppel, IEEE Trans. Microw. Theory Tech. **50**, 738 (2002).
[2] E. A. Cerda-Méndez, D. Sarkar, D. N. Krizhanovskii, S. S. Gavrilov, K. Biermann, M. S. Skolnick, and P. V. Santos, Phys. Rev. Lett. **111**, 146401 (2013).
[3] C. Ruppert, J. Neumann, J. B. Kinzel, H. J. Krenner, A. Wixforth, and M. Betz, Phys. Rev. B **82**, 081416 (2010).
[4] J. Schiefele, J. Pedrós, F. Sols, F. Calle, and F. Guinea, Phys. Rev. Lett. **111**, 237405 (2013).
[5] P. V. Santos, T. Schumann, M. H. Oliveira, J. M. J. Lopes, and H. Riechert, Appl. Phys. Lett. **102**, 221907 (2013).
[6] V. Miseikis, J. E. Cunningham, K. Saeed, R. O'Rorke, and A. G. Davies, Appl. Phys. Lett. **100**, 133105 (2012).
[7] L. Bandhu, L. M. Lawton, and G. R. Nash, Appl. Phys. Lett. **103**, 133101 (2013).
[8] P. Thalmeier, B. Dóra, and K. Ziegler, Phys. Rev. B **81**, 041409 (2010).
[9] A. H. Castro Neto, F. Guinea, N. M. R. Peres, K. S. Novoselov, and A. K. Geim, Rev. Mod. Phys. **81**, 109 (2009).
[10] A. C. Ferrari *et al.*, Nanoscale **7**, 4598 (2015).
[11] K. Bolotin, K. Sikes, Z. Jiang, M. Klima, G. Fudenberg, J. Hone, P. Kim, and H. Stormer, Solid State Commun. **146**, 351 (2008).
[12] R. C. Dean, A. F. Young, I. Meric, C. Lee, L. Wang, S. Sorgenfrei, K. Watanabe, T. Taniguchi, P. Kim, K. L. Shepard, and J. Hone, Nat. Nanotechnol. **5**, 722 (2010).
[13] S. Fratini and F. Guinea, Phys. Rev. B **77**, 195415 (2008).
[14] J.-H. Chen, C. Jang, S. Xiao, M. Ishigami, and M. S. Fuhrer, Nat. Nanotechnol. **3**, 206 (2008).
[15] K. Zou, X. Hong, D. Keefer, and J. Zhu, Phys. Rev. Lett. **105**, 126601 (2010).
[16] J. Schiefele, F. Sols, and F. Guinea, Phys. Rev. B **85**, 195420 (2012).
[17] B. Amorim, J. Schiefele, F. Sols, and F. Guinea, Phys. Rev. B **86**, 125448 (2012).
[18] Z.-Y. Ong and M. V. Fischetti, Phys. Rev. B **86**, 165422 (2012).
[19] Z.-Y. Ong and M. V. Fischetti, Appl. Phys. Lett. **102**, 183506 (2013).
[20] Z.-Y. Ong and M. V. Fischetti, Phys. Rev. B **88**, 045405 (2013).
[21] E. H. Hwang and S. Das Sarma, Phys. Rev. B **87**, 115432 (2013).
[22] H. Ezawa, Ann. Phys. (N.Y.) **67**, 438 (1971).
[23] W.-K. Tse, E. H. Hwang, and S. Das Sarma, Appl. Phys. Lett. **93**, 023128 (2008).
[24] X. Hong, A. Posadas, K. Zou, C. H. Ahn, and J. Zhu, Phys. Rev. Lett. **102**, 136808 (2009).
[25] S. Bidmeshkipour, A. Vorobiev, M. A. Andersson, A. Kompany, and J. Stake, Appl. Phys. Lett. **107**, 173106 (2015).
[26] Q. Li and S. Das Sarma, Phys. Rev. B **87**, 085406 (2013).
[27] G. D. Mahan, *Many-Particle Physics* (Springer Science & Business Media, Boston, 2013).
[28] S. H. Simon, Phys. Rev. B **54**, 13878 (1996).
[29] D. G. González, F. Sols, F. Guinea, and I. Zapata, Phys. Rev. B **94**, 085423 (2016).
[30] B. Wunsch, T. Stauber, F. Sols, and F. Guinea, New J. Phys. **8**, 318 (2006).
[31] E. H. Hwang and S. Das Sarma, Phys. Rev. B **75**, 205418 (2007).
[32] R. D. Mattuck, *A Guide to Feynman Diagrams in the Many-Body Problem* (Courier, New York, 2012).
[33] D. Royer and E. Dieulesaint, *Elastic Waves in Solids I: Free and Guided Propagation* (Springer Science & Business Media, Berlin, 2000).
[34] B. Auld, *Acoustic Fields and Waves in Solids* (Krieger, Malabar, 1990).
[35] A. Knäbchen, Y. B. Levinson, and O. Entin-Wohlman, Phys. Rev. B **54**, 10696 (1996).
[36] J. Pedrós, L. García-Gancedo, C. J. B. Ford, C. H. W. Barnes, J. P. Griffiths, G. A. C. Jones, and A. J. Flewitt, J. Appl. Phys. **110**, 103501 (2011).
[37] A. Wixforth, J. Scriba, M. Wassermeier, J. P. Kotthaus, G. Weimann, and W. Schlapp, Phys. Rev. B **40**, 7874 (1989).
[38] J. Campbell and W. Jones, IEEE Trans. Sonics Ultrason. **15**, 209 (1968).
[39] R. S. Weis and T. K. Gaylord, Appl. Phys. A **37**, 191 (1985).
[40] S. Sanna and W. G. Schmidt, Phys. Rev. B **81**, 214116 (2010).
[41] W.-K. Tse and S. Das Sarma, Phys. Rev. Lett. **99**, 236802 (2007).
[42] K. Kaasbjerg, K. S. Thygesen, and K. W. Jacobsen, Phys. Rev. B **85**, 165440 (2012).
[43] S. H. Zhang, W. Xu, S. M. Badalyan, and F. M. Peeters, Phys. Rev. B **87**, 075443 (2013).
[44] A. B. Migdal, Sov. Phys. JETP **34**, 996 (1958).
[45] S. Das Sarma, E. H. Hwang, and W.-K. Tse, Phys. Rev. B **75**, 121406 (2007).
[46] E. B. Song, B. Lian, S. M. Kim, S. Lee, T.-K. Chung, M. Wang, C. Zeng, G. Xu, K. Wong, Y. Zhou, H. I. Rasool, D. H. Seo, H.-J. Chung, J. Heo, S. Seo, and K. L. Wang, Appl. Phys. Lett. **99**, 042109 (2011).